JOURNAL OF THERMOPHYSICS AND HEAT TRANSFER
Vol. 19, No. 1, January–March 2005

Skin-Temperature Prediction of Aircraft Rear Fuselage with Multimode Thermal Model

S. P. Mahulikar,* P. S. Kolhe,† and G. A. Rao‡
Indian Institute of Technology, Bombay 400 076, India

The temperature distribution of the exposed rear fuselage of fighter aircraft, which is necessary for estimating passively emitted infrared signature levels, is predicted. Hot combustion gases flowing through the gas-turbine engine and aerodynamic heating of the rear fuselage at high freestream Mach numbers are the two heat sources. Turbulent forced convection and radiation are the dominant heat-transfer modes, and hence two thermal models are developed: only turbulent forced convection, and combined turbulent forced convection and radiation. Variation in transport and thermophysical properties of fluids is also modeled. Gas-dynamic equations are used to obtain local flow parameters, considering the role of friction, heat transfer, and area variation. A radiation-shape-factor analysis for the complete layout is presented that accounts for mutual, partial, or complete visibility of emitter and receiver elements. A closed-form solution for shape factors between ring elements is derived for the annulus. The error in temperature estimation by neglecting parameters such as aerodynamic heating, variation in transport, and thermophysical and local-flow properties of fluid is found to be significant. We conclude with a discussion of the role of altitude and flight Mach number.

Nomenclature

A = area, m^2
a–i = terms involved in integration
B = radiance, W/m^2
Bi = Biot number
C_p = specific heat at constant pressure, J/kg K
D = diameter of duct, m
D_h = hydraulic diameter, m
dA = area of elemental strip, m^2
dx = width of elemental strip, m
F = shape factor (angle factor, configuration factor, view factor)
f = friction factor in gas-dynamic equations
H = irradiance, W/m^2
h = convective-heat-transfer coefficient, W/m^2 K
K_T = thermal conductivity of fluid, W/m K
L = distance between disks under consideration, m
l = distance between elemental areas on emitter and receiver elements, m
M = Mach number
$\dot{m}$ = mass flow rate, kg/s
N = number of elements
P = pressure, Pa
Q = total enthalpy, J
q = heat flow rate, W
R = gas constant for air, 287 J/kg K
R_a, R_b = radius of disk, m
R_i, R_o = inner and outer radius of annular disk, m
r = radius of blocking section, m
r_1, r_2 = radius of element, m
T = temperature, K
T_R = recovery temperature, K
T_s = Sutherland's constant, K
v = velocity of fluid, m/s
X = coefficient of change in area term in gas-dynamics equation
x = distance between elements, m
Y = coefficient of heat-transfer term in gas-dynamics equation
Z = coefficient of friction-loss term in gas-dynamics equation
α = blockage (or shadow) angle, rad
β = angle between normal and line joining elemental areas, rad
γ = ratio of specific heats of fluid
Δ = increment operator
δ = axial width of element, m
ε = emissivity
η = surface orientation angle, rad
θ = azimuth angle for emitter element, rad
μ = dynamic viscosity, Pa s
ρ = density, kg/m^3
Σ = summation operator
σ = Stefan–Boltzmann constant, 5.67×10^{-8} W/m^2 K^4
ϕ = azimuth angle for receiver element, rad

Subscripts

a, b = disk element
c = convective-heat-transfer mode
c/s = based on cross section
disk = annular disk element
F = fluid
ID = inlet disk
in, ou = at inner or outer surfaces, respectively
k = element number
mix = after mixture of two ram airflows
OD = outlet disk
P = based on pressure
r = radiation
ref = reference quantity
S1–S6 = wall surfaces
sky = sky (ambience for radiation)
surf = over all visible surfaces
T = based on temperature
W = duct wall

Received 6 November 2003; revision received 25 May 2004; accepted for publication 26 May 2004.

*Faculty Member and A. von Humboldt Fellow, Department of Aerospace Engineering, P.O. IIT, Powai. spm@aero.iitb.ac.in.

†Senior Research Assistant, Department of Aerospace Engineering, P.O. IIT, Powai.

‡Research Scholar, Department of Aerospace Engineering. P.O. IIT, Powai.

0 = total condition
1, 2 = element under consideration
I = duct wall of jet pipe with convergent–divergent (C–D) nozzle or exhaust gas
II = radiation shield or ram airflow between jet pipe and radiation shield
III = rear fuselage or ram airflow between rear fuselage and radiation shield
IV = freestream flow
∞ = ambient conditions

Introduction

ADVANCES in aircraft-detection technology and antiaircraft defense systems have necessitated the development of low-observables technology for increasing aircraft survivability, in order to maintain air superiority.[1] Stealth technology aims at reducing detectability of aircraft, both by active techniques such as radar and by passive techniques such as infrared detection.[1] Infrared (IR) signatures are produced by contrast in IR emission between aircraft surface and background sky/atmosphere. The power plant is the most significant source of IR signature in aircraft because it acts as a graybody and emits radiation throughout the IR spectrum. Hot combustion gases flowing through the engine and aerodynamic heating of the rear fuselage at high Mach number are the two heat sources for aircraft rear fuselage. Thus, the main modes of heat transfer are turbulent forced convection and surface radiation interchange.

The prime motivation behind this analytical and computational exercise is the fact that dynamic experiments with aircraft engines for estimation of skin temperatures of rear fuselage, under various flight and engine operating conditions, not only are prohibitively expensive but also are difficult to implement practically. Experimental data on engine test bed/ground runs are not available in the literature. There exists a pressing need to develop the capability to predict skin temperature of aircraft rear fuselage as accurately as possible, to enable infrared-signature studies.

Literature review of heat transfer for flow through pipes by turbulent forced convection reflects that most investigators used the finite-difference equations for conservation of energy, x-momentum, and continuity, and have emphasized modeling of variation in fluid transport properties. Bankston and McEligot[2] predicted wall-temperature and pressure drops for strongly heated forced internal flows and used constant power-law index approximation for modeling variation in transport properties. Malik and Pletcher,[3] Pletcher,[4] and Pletcher and Malik[5] predicted the turbulent-flow heat transfer in annular geometries with property variations, in which they considered the flow to be axisymmetric, steady, and fully turbulent. Some investigators also studied combined forced convection and radiation for flow inside conduits, either considering surface radiation alone or surface radiation with optically active gas.[6,7] The general methodology is to discretize the layout and solve energy-balance equations for fluid and wall elements simultaneously. Correlations for estimating convective heat flux are used instead of solving the governing fluid-flow conservation equations with turbulence modeling. Mahulikar et al.[8] and Mahulikar[9] predicted the engine casing temperature of fighter aircraft using a combined convective and radiative heat transfer approach. They treated the aircraft engine layout as three coaxial cylinders and a flow of optically transparent gas bounded by gray walls for modeling. They have not considered aerodynamic heating by the freestream and variation of fluid properties with temperature and pressure. The governing conservation equations comprise energy, mass, and momentum balance for each fluid element and heat-balance equations for wall elements. They discretized the engine layout axially and used the Newton–Raphson method to arrive at the steady-state axial temperature distribution of the three internal fluid flows and walls.

Shape factors are required for analytical formulation of the radiant heat exchange process. The construction and surface orientation of the engine layout impose restrictions on visibility of surfaces. The methods proposed to date by various investigators for finding the shape factors with blockage effect are based on integration. Eddy and Neilsson[10] analyzed the radiation shape factors for varying cross sections, which can be applied to the jet pipe and convergent–divergent (C–D) nozzle. The integral used is the one proposed by Robin,[11] which is applicable to surfaces of revolution. The method of finding integration limits proposed by Eddy and Neilsson[10] is applicable to small-axial-width elements. From the viewpoint of radiation heat exchange analysis in annular geometry, the radiation shape factors for finite-length coaxial circular cylinders, conical cavities, and coaxial axisymmetric geometries are important. Many investigators have contributed to the literature in this regard. Tso and Mahulikar,[12] Reid and Tennant,[13] and Brockmann[14] dealt with the geometry of coaxial cylinders. Saltiel and Naraghi,[15] Chung et al.,[16] and Modest[17] dealt with coaxial axisymmetric bodies, whereas Nunes and Naraghi[18] and Nunes et al.[19] developed a numerical model for axisymmetric geometries with gaseous radiative participating media.

Objective and Scope

In the present work, gas-dynamic equations are used to obtain temperature and pressure distributions of the fluids in the engine layout. The complication involved in modeling radiative heat transfer is the radiation-shape-factor analysis. The problem is aggravated if the layout comprises annular ducts of unequal length and varying cross section, because the methodology of radiation-shape-factor analysis in such cases is not available in literature. A detailed radiation-shape-factor analysis is provided for solving radiative heat transfer problems encountered in complicated geometries such as that of a gas turbine engine. Mahulikar et al.[8] and Mahulikar[9] approximated aircraft engine layouts as three coaxial cylinders and did not consider variation in thermophysical and transport properties of fluid with temperature. In this investigation, both these issues are dealt with, and the error in temperature estimation is presented.

The entire analysis is for a gas-turbine engine in the "dry mode" (non afterburning), because fighter aircraft use afterburners for a short duration of their mission. The fuel–air ratio in gas turbine engines is very lean, and hence the molar fractions of radiatively participating gases such as CO_2, H_2O, and CO is less, and their impact on net heat transfer is not significant. Besides, these gases being selective emitters and at relatively low temperatures (<900 K), gas radiation is not comparable to that from wall surfaces, which act like gray bodies (by emitting radiation at all wavelengths at all temperatures). Hence, in the present analysis, gas radiation heat exchange is not modeled. It is only at high temperatures incurred in the afterburning mode that gas radiation interchange is dominant and may increase the total wall heat-flux by about 20–30%. Modeling the heat-transfer process requires information about the constructional features, geometrical layout, and fluid-flow path of the engine. Here two generic engine layouts are considered (Figs. 1 and 2); layout 2 is a special case of layout 1, in which the radiation shield extends up to the end of the C–D nozzle. This typical engine layout comprises three coaxial ducts with exhaust gases flowing through the core, ram air flowing through the annulus, and freestream flow over the outermost duct. The innermost duct is the jet pipe and C–D nozzle, the intermediate duct is the shroud, which serves as a radiation shield, and the outermost duct is the rear fuselage skin of the aircraft.

The two heat sources for the rear fuselage are the hot combustion products flowing through the jet pipe and the freestream, which may act as either a heat source or a heat sink, depending on the flight altitude Mach number. Generally, the ducts are thin and have $Bi < 0.1$; hence, the radial temperature difference is neglected. Because the Nusselt numbers are generally high due to turbulent flows, temperature change due to axial conduction through the ducts is negligible as compared to the axial temperature change due to convection. Hence, conduction modeling through the ducts is excluded. Because of the highly turbulent nature of the flow, the fluid is well mixed in the radial and circumferential directions. Hence, the variation in temperature of fluids and ducts is modeled only axially. As the temperature of the exhaust gases flowing through the jet pipe is relatively high ($\sim$1000 K in the dry mode), radiation heat interchange is significant. Hence, the thermal model developed comprises two modes of heat transfer: turbulent forced convection and surface radiation.

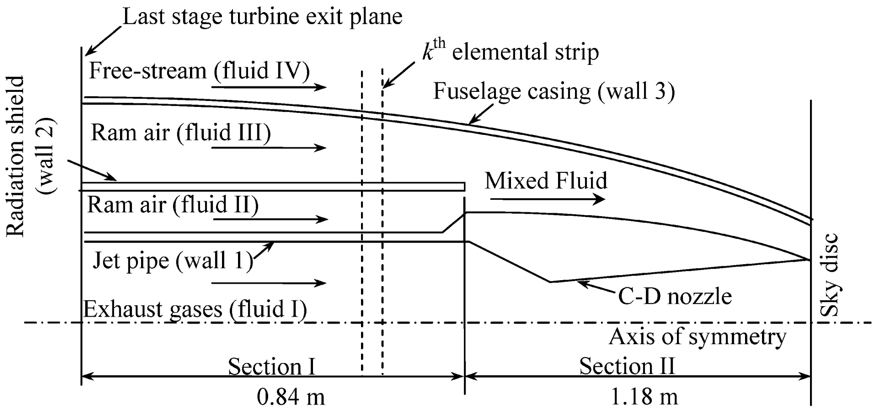

Fig. 1 Schematic of aircraft engine layout 1.

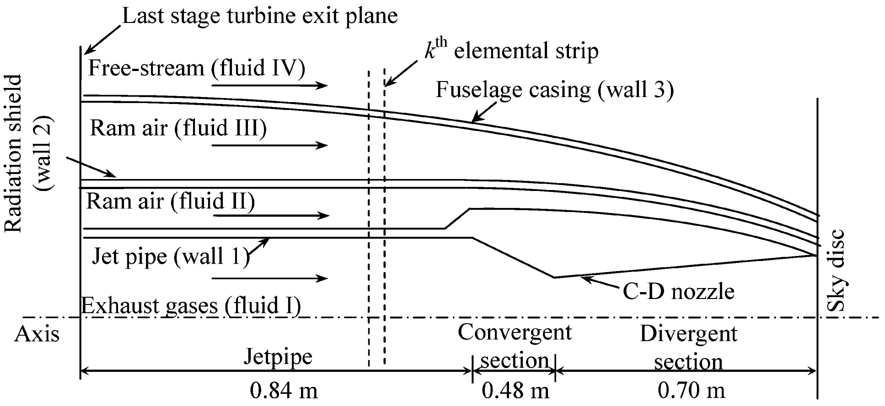

Fig. 2 Schematic of aircraft engine layout 2.

Analytical solution is ruled out due to joint radiation and convection, resulting in a nonlinear system. Hence, a zonal method is used, where the engine layout is axially discretized into a certain number of elements. For the present study, the whole layout is discretized into 30 elements for the zonal analysis, comprising 10 equal elements each for the jet pipe, convergent nozzle section, and divergent nozzle section. The governing equations for the combined turbulent forced convection and radiation model mainly include the heat-balance equations for the duct wall elements: For the kth element of the duct wall, in section I,

$$q_{c,F\text{I},W\text{I},k} + q_{c,F\text{II},W\text{I},k} + q_{r,\text{S}1,k} + q_{r,\text{S}2,k} = 0 \tag{1}$$

$$q_{c,F\text{II},W\text{II},k} + q_{c,F\text{III},W\text{II},k} + q_{r,\text{S}3,k} + q_{r,\text{S}4,k} = 0 \tag{2}$$

$$q_{c,F\text{III},W\text{III},k} + q_{c,F\text{IV},W\text{III},k} + q_{r,\text{S}5,k} + q_{r,\text{S}6,k} = 0 \tag{3}$$

and in section II,

$$q_{c,F\text{I},W\text{I},k} + q_{c,F\text{mix},W\text{I},k} + q_{r,\text{S}1,k} + q_{r,\text{S}2,k} = 0 \tag{4}$$

$$q_{c,F\text{mix},W\text{I},k} + q_{c,F\text{IV},W\text{III},k} + q_{r,\text{S}5,k} + q_{r,\text{S}6,k} = 0 \tag{5}$$

The respective fluid and wall temperatures are assumed constant within an axially discretized element and assigned at center. The boundary conditions are gas-inlet temperatures and pressures, freestream parameters, and convective heat transfer coefficients. The radiation boundary conditions are the emissivities of all surfaces and the temperatures of inlet and exit discs defining the enclosures. Steady-state forced convective heat transfer is modeled over all surfaces, in conjunction with radiation interchange between these surfaces and radiation heat loss to the sky. To evaluate the heat-flow rates in the heat-balance equations, the radiative heat flow rates are calculated as the difference between the radiance and irradiance terms, whereas convective heat flow rates are calculated using the convective heat transfer coefficients:

$$q_{ck} = h_k \cdot A_k \cdot (T_{Wk} - T_{Fk}) \tag{6}$$

$$q_{rk} = A_k \cdot (B_k - H_k) \tag{7}$$

The radiance terms in the radiative heat flux equation are given by

$$B_k = \varepsilon_k \cdot \sigma \cdot (T_k)^4 + (1 - \varepsilon_k) \cdot H_k \tag{8}$$

The irradiance on the inlet disk, fuselage outer surface, and remaining duct surfaces is given by

$$H_{\text{ID}} = \sum_{\text{surf}} \left[\sum_{k=1}^{N} (A_k \cdot F_{k-\text{ID}} \cdot B_k)_{\text{surf}} \right] \tag{9}$$

$$H_k = \sigma \cdot (T_{\text{sky}})^4 \tag{10}$$

$$H_k = \sum_{\text{surfaces}} \left\{ \left[\sum_{l=1}^{N} F_{k-l} \cdot B_l \right] \right\} + F_{k-\text{ID}} \cdot B_{\text{ID}} + F_{k-\text{OD}} \cdot B_{\text{OD}} \tag{11}$$

respectively. At the start of section II, adiabatic and instantaneous mixing of the two fluid streams of ram air (fluid II and fluid III) is assumed because of their highly turbulent nature. Because a large velocity difference exists between the two ram airflows, conservation of mass [Eqs. (12)], conservation of energy [Eq. (13)], and conservation of momentum [Eq. (14)] are used[20] to compute the temperature, pressure, and Mach number at the entry plane of section II:

$$\dot{m}_{F\text{II}} + \dot{m}_{F\text{III}} = \dot{m}_{F\text{mix}} \tag{12a}$$

$$\dot{m}_{F\mathrm{II}} = \rho_{F\mathrm{II},k} \cdot A_{Ck,W\mathrm{II}} \cdot v_{F\mathrm{II},k} \tag{12b}$$

$$\dot{m}_{F\mathrm{III}} = \rho_{F\mathrm{III},k} \cdot A_{Ck,W\mathrm{III}} \cdot v_{F\mathrm{III},k} \tag{12c}$$

$$\dot{m}_{F\mathrm{mix}} = \rho_{F\mathrm{mix},k} \cdot A_{Ck,W\mathrm{mix}} \cdot v_{F\mathrm{mix},k} \tag{12d}$$

$$\dot{m}_{F\mathrm{mix}} \cdot C_{p,F\mathrm{mix}} \cdot T_{0,F\mathrm{mix}} = \dot{m}_{F\mathrm{II}} \cdot C_{p,F\mathrm{II}} \cdot T_{0,F\mathrm{II}} + \dot{m}_{F\mathrm{III}} \cdot C_{p,F\mathrm{III}} \cdot T_{0,F\mathrm{III}} \tag{13}$$

$$(\dot{m}_{F\mathrm{mix}} \cdot v_{F\mathrm{mix}} + A_{C,F\mathrm{mix}} \cdot P_{F\mathrm{mix}})_{\mathrm{sectIIs}} = (\dot{m}_{F\mathrm{II}} \cdot v_{F\mathrm{II}} + A_{C,F\mathrm{II}} \cdot P_{F\mathrm{II}} + \dot{m}_{F\mathrm{III}} \cdot v_{F\mathrm{III}} + A_{C,F\mathrm{III}} \cdot P_{F\mathrm{III}})_{\mathrm{sectIe}} \tag{14}$$

To avoid discrepancies in the convective heat flow rates, the thermophysical and transport properties are evaluated at local fluid temperature and pressure. To evaluate the local fluid flow properties, gas-dynamic equations are used that take into account the effect of heat transfer, change in area, and friction on fluid temperature and pressure. The flow-Mach-number variation is evaluated from the continuity equation. Equations (15) and (16) give the temperature and pressure variations across a fluid element,[21] whereas Eq. (17) gives the Mach number at the outlet of a fluid element:

$$(\mathrm{d}T_{Fk}/T_{Fk}) = -X_{TFk} \cdot (\mathrm{d}A_{Ck}/A_{Ck}) - Y_{TFk} \cdot [\Delta Q_{Fk}/(R \cdot T_{Fk})] + Z_{TFk} \cdot [f_{Fk} \cdot \mathrm{d}x/D_h] \tag{15a}$$

$$X_{TFk} = \left[(\gamma - 1) \cdot M_{F(k-1)}\right] \Big/ \left[\left(M_{F(k-1)}\right)^2 - 1\right] \tag{15b}$$

$$Y_{TFk} = \left[1 - \gamma \cdot \left(M_{F(k-1)}\right)^2\right] \cdot (\gamma - 1) \Big/ \left\{\gamma \cdot \left[\left(M_{F(k-1)}\right)^2 - 1\right]\right\} \tag{15c}$$

$$Z_{TFk} = \left[\gamma \cdot (\gamma - 1) \cdot \left(M_{F(k-1)}\right)^4\right] \Big/ \left\{2\left[\left(M_{F(k-1)}\right)^2 - 1\right]\right\} \tag{15d}$$

$$(\mathrm{d}P_{Fk}/P_{Fk}) = -X_{PFk} \cdot (\mathrm{d}A_{Ck}/A_{Ck}) - Y_{PFk} \cdot [\Delta Q_{Fk}/(R \cdot T_{Fk})] + Z_{PFk} \cdot [f_{Fk} \cdot \mathrm{d}x/D_h] \tag{16a}$$

$$X_{PFk} = \left[\gamma \cdot \left(M_{F(k-1)}\right)^2\right] \Big/ \left[\left(M_{F(k-1)}\right)^2 - 1\right] \tag{16b}$$

$$Y_{PFk} = \gamma \cdot \left(M_{F(k-1)}\right)^2 \cdot (\gamma - 1) \Big/ \left\{\gamma \cdot \left[\left(M_{F(k-1)}\right)^2 - 1\right]\right\} \tag{16c}$$

$$Z_{PFk} = \gamma \cdot \left(M_{F(k-1)}\right)^2 \cdot \left[1 + (\gamma - 1) \cdot \left(M_{F(k-1)}\right)^2\right] \Big/ \left\{2\left[\left(M_{F(k-1)}\right)^2 - 1\right]\right\} \tag{16d}$$

$$M_{Fk} = \dot{m} \cdot (R \cdot T_{Fk}/\gamma)^{\frac{1}{2}} \Big/ (P_{Fk} \cdot A_{Ck}) \tag{17}$$

The change in enthalpy per unit mass of fluid across a fluid element is required as an input to the gas-dynamic equations; it is given by the enthalpy balance of a fluid element:

$$\Delta Q_{Fk} = C_{p,Fk} \cdot \left(T_{0,F(k+1)} - T_{0,Fk}\right) = \left(\sum_{\mathrm{surfaces}} \dot{q}_{cFW}\right)_k \Big/ \dot{m}_F \tag{18}$$

Equation (19) gives the expression for the friction factor for flow through smooth pipes based on the Reynolds number:[22]

$$f = \left[\left\{1.82 \log\left[\rho \cdot M \cdot (\gamma \cdot R \cdot T)^{\frac{1}{2}}\right] \cdot D_h \Big/ \mu\right\} - 1.64\right]^{-2} \Big/ 4 \tag{19}$$

The Mach number is unity at throat of the nozzle (i.e., sonic condition). If the sonic condition is reached at the first element of the divergent nozzle section, the resulting singularity requires the solution of conservation of mass, momentum, and energy equations iteratively to obtain temperature, pressure, and Mach number variation across the element. The adiabatic wall temperature for heat transfer with the freestream flow is the recovery temperature, which for the turbulent boundary layer is given as[23]

$$T_R = T_\infty \cdot \left\{1 + (\mu \cdot C_p/k_T)^{\frac{1}{3}} \cdot [(\gamma - 1)/2] \cdot (M_\infty)^2\right\} \tag{20}$$

The Dittus–Boelter equation is used to calculate the convective heat transfer coefficient for internal flows:

$$(h \cdot D/K_T) = 0.023(\rho \cdot v \cdot D/\mu)^{0.8} \cdot (\mu \cdot C_p/K_T)^n \tag{21}$$

where the exponent $n = 0.3$ when fluid is being cooled, and $n = 0.4$ when fluid is being heated. For the annular flow, the hydraulic diameter is used to evaluate the convective heat transfer coefficient. The Nusselt number correlation for flow over a flat plate is used to calculate the convective heat transfer coefficient for freestream flow and is given as[23]

$$h = 0.0366\left\{\rho \cdot M \cdot L \cdot (\gamma \cdot R \cdot T)^{\frac{1}{2}} \Big/ \mu\right\}^{0.8} \cdot \left[(\mu \cdot C_p/K_T)^{\frac{1}{3}} \cdot K_T \Big/ L\right] \tag{22}$$

The variation in fluid properties with temperature is estimated to reduce discrepancies in the convective heat flux calculation. Sutherland's law is used to model $\mu(T_F)$ as

$$\mu(T_F) = \mu_{\mathrm{ref}} \cdot (T_F/T_{\mathrm{ref}})^{\frac{3}{2}} \cdot (T_{\mathrm{ref}} + T_s)/(T_F + T_s) \tag{23}$$

The variations $C_p(T_F)$, $\gamma(T_F)$, and $K_T(T_F)$ are taken from standard data tables. The governing equations for modeling turbulent forced convection are the same for both models (convection and combined convection and radiation).

Numerical Solution Methodology

The governing equations include heat-balance equations for all elements and expressions for evaluating various terms involved in these equations. The Newton–Raphson method and the method of successive substitution[24] are two popular methods for solving such systems of nonlinear equations. The latter method is adopted here wherein some variables are assigned initial values, and then proceeding through the system of equations, all variables are recalculated and successively substituted until satisfactory convergence is achieved. Figure 3 illustrates the flowchart of the solution scheme used. In this method, the sequence of calculation of various variables is important, and the convergence criterion used controls the error in the heat-flux balance of the elements. For the present study, a convergence criterion based on maximum difference in updated values between two successive iterations of 10^{-4} is used for temperature, and 10^{-3} is used for heat balance for all discretized elements.

Radiation-Shape-Factor Analysis

Radiation shape factors are key elements in the solution of the energy equations with surface radiation interchange. The radiation-shape-factor analysis is carried out separately for jet pipe with a C–D nozzle and for annular ducts. All surfaces are considered as diffuse, opaque, and grey; these assumptions are valid because the wall surfaces are oxidized by the engine operating environment. The shape factor depends only on geometry and orientation of surfaces. Because zonal analysis is applied, the duct walls are divided into a number of ring elements, either cylindrical or conical frustum.

Radiation-Shape-Factor Analysis for Jet Pipe with Convergent–Divergent Nozzle

In this configuration (Fig. 4), elements that lie on the same side of the throat are mutually visible, whereas elements lying on the other side of the throat are partially visible to each other due to blockage by the throat. The various cases of shape factor that arise for this configuration are discussed.

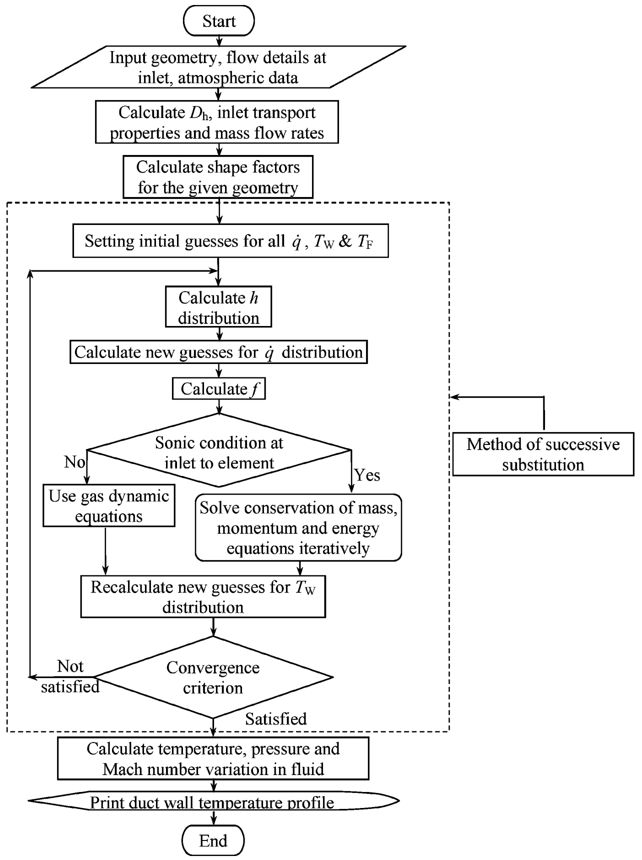

Fig. 3 Flowchart for the numerical solution method.

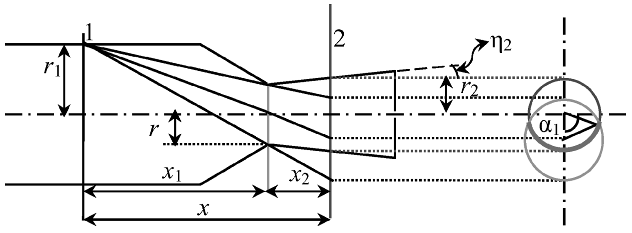

Fig. 4 Two ring elements of jet pipe and C–D nozzle with blockage effect.

Ring Element to Any Other Ring Element

To obtain this shape factor, a generalized single integration is performed, which is derived from the basic quadruple line integral of shape factors. The quadruple line integral involves two integrals over the azimuth angle and two integrals over the axial width of the elements (because the radius of elements varies with the axial width for the conical frustum ring element), and is given by[17]

$$F_{1-2} = \frac{1}{A_1} \cdot \int_0^{2\pi} \int_0^{\delta_1} \int_0^{\delta_2} \int_{\varphi_i}^{\varphi_o} \frac{\cos(\beta_1) \cdot \cos(\beta_2)}{\pi \cdot l^2} \cdot r_1 \cdot r_2 \cdot \mathrm{d}\varphi \cdot \frac{\mathrm{d}x_2}{\cos(\eta_2)} \cdot \frac{\mathrm{d}x_1}{\cos(\eta_1)} \cdot \mathrm{d}\theta \tag{24}$$

The fine axial discretization of the layout ensures that variation in the azimuth-angle integration limit over the axial width of the element is insignificant, and hence two line integrals over the axial width can be eliminated. The geometry being axisymmetric, the line integral over the azimuth angle of the emitter element (of the two elements under consideration) can be solved by symmetry and hence the quadruple line integral reduces to a single integral, given as

$$F_{1-2} = \frac{r_2 \cdot \delta_2}{\cos(\eta_2)} \int_{\varphi_i}^{\varphi_o} \frac{\cos(\beta_1) \cdot \cos(\beta_2)}{\pi \cdot l^2} \cdot \mathrm{d}\varphi \tag{25}$$

Solving this integral, $F_{1-2} = G(\phi_o) - G(\phi_i)$, where the function $G(\phi)$ is given as

$$G(\varphi) = 2 \cdot \mathrm{d} \cdot \left\{e \cdot f \cdot g + [(c^2 - 1) \cdot f \cdot \varphi/2 - \tan(\varphi/2) \cdot (c - a) \cdot (b - c)] \cdot \sqrt{c^2 - 1}\right\} \Big/ \left[(c^2 - 1)^{\frac{3}{2}} \cdot f\right] \tag{26a}$$

where

$$a = (r_1 - x \cdot \tan\eta_1)/r_2 \tag{26b}$$

$$b = (r_2 - x \cdot \tan\eta_2)/r_1 \tag{26c}$$

$$c = \left[r_1^2 + r_2^2 + x^2\right] \big/ (2r_1 \cdot r_2) \tag{26d}$$

$$d = \cos\eta_1 \cdot \delta_2/(2\pi \cdot r_1) \tag{26e}$$

$$e = (-c^3 + a \cdot b \cdot c + 2c - a - b) \tag{26f}$$

$$f = (c + 1) \cdot \tan^2(\phi/2) + c - 1 \tag{26g}$$

$$g = \tan^{-1}\left[(c + 1) \cdot \tan(\phi/2)/(c^2 - 1)^{\frac{1}{2}}\right] \tag{26h}$$

In Eq. (26), η_1 and η_2 are the surface orientation angles for emitter and receiver elements, respectively. The sign conventions while moving in the direction from emitter element to receiver element are as follows: if the emitter element is in the convergent section, η_1 is positive, otherwise negative; if the receiver element is in the divergent section, η_2 is positive, otherwise negative. The integration limits ϕ_o and ϕ_i for the ring elements having no blockage are π and zero, respectively. For elements that are partially visible, the integration limits can be found by light-ray projection of the blocking section onto the plane of the receiver element (see Fig. 4), and are $\phi_i = \pi - \mathrm{Min}(\alpha_1, \alpha_2)$ and $\phi_o = \pi$, where

$$\alpha_1 = \cos^{-1}\left\{\left[r_1^2 \cdot x_2^2 - r^2 \cdot x^2 + r_2^2 \cdot x_1^2\right] \big/ (2r_1 \cdot r_2 \cdot x_1 \cdot x_2)\right\} \tag{27a}$$

$$\alpha_2 = \cos^{-1}[(r_2 - x \cdot \tan\eta_2)/r_1] \tag{27b}$$

The α_1 considers the blockage due to the throat, whereas α_2 considers the blockage due to self-orientation of rings (i.e., $\cos\beta_2 = \pi/2$ limits the visibility). The plane of the receiver element considered for finding the integrating limits passes through the center of the axial width of the element.

The integral developed above is applicable to elements with small axial width; hence, to increase the accuracy of ring-element-to-ring-element shape factors, each discretized element is further divided. Shape-factor algebra is then used to recalculate the original ring element to ring-element shape factor.

Ring Element with Itself

These shape factors are evaluated using the disk-to-disk shape factor, conservation of energy, and shape-factor algebra. The shape factor between two disks separated by a distance L (shown in Fig. 5) is given in Ozisik[25] as

$$F_{a-b} = \left(R_a^2 + R_b^2 + L^2 - \sqrt{\left(R_a^2 + R_b^2 + L^2\right)^2 - 4 \cdot R_a^2 \cdot R_b^2}\right) \Big/ 2R_a^2 \tag{28}$$

By the law of conservation of energy, by the reciprocity rule, and because flat or convex surfaces cannot see themselves,

$$F_{a-k} = 1 - F_{a-b} \tag{29}$$

$$F_{b-k} = 1 - (A_a/A_b) \cdot F_{a-b} \tag{30}$$

$$F_{k-k} = 1 - (F_{k-a} + F_{k-b}) \tag{31a}$$

$$F_{k-a} = (A_a/A_k) \cdot F_{a-k} \tag{31b}$$

$$F_{k-b} = (A_b/A_k) \cdot F_{b-k} \tag{31c}$$

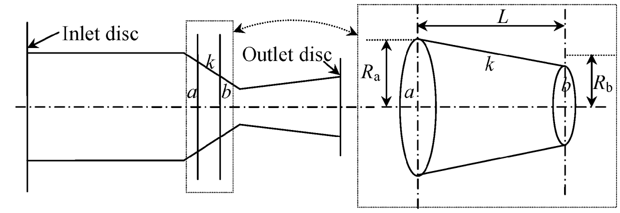

Fig. 5 Generalized element of the jet pipe and C–D nozzle.

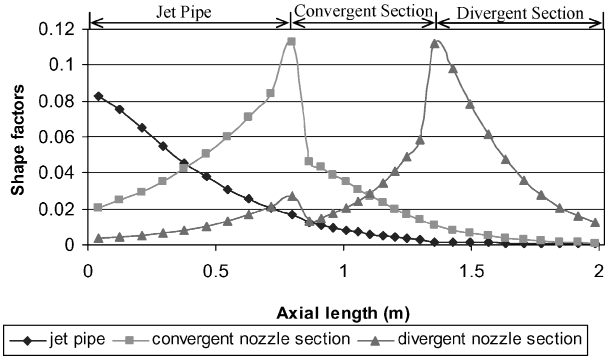

Fig. 6 Ring-element-to-ring-element shape factors for jet pipe with C–D nozzle.

Using Eqs. (28–31), the shape factor for any generalized element with respect to itself is given by

$$F_{k-k} = 1 - \left(\begin{array}{l} (A_a/A_k)\cdot\left\{1 - \left[R_a^2 + R_b^2 + L^2 - \sqrt{\left(R_a^2 + R_b^2 + L^2\right)^2 - 4\cdot R_a^2\cdot R_b^2}\right]\Big/2R_a^2\right\} \\ + (A_b/A_k)\cdot\left\{1 - \left[R_a^2 + R_b^2 + L^2 - \sqrt{\left(R_a^2 + R_b^2 + L^2\right)^2 - 4\cdot R_a^2\cdot R_b^2}\right]\Big/2R_b^2\right\} \end{array} \right) \tag{32}$$

Ring Element to Inlet and Outlet Disk

From Eqs. (28–31), the shape factor of the ring element with left and right disk is calculated as

$$F_{k-a} = (A_a/A_k)\cdot\left\{1 - \left[R_a^2 + R_b^2 + L^2 - \sqrt{\left(R_a^2 + R_b^2 + L^2\right)^2 - 4\cdot R_a^2\cdot R_b^2}\right]\Big/2R_a^2\right\} \tag{33}$$

$$F_{k-b} = (A_b/A_k)\cdot\left\{1 - \left[R_a^2 + R_b^2 + L^2 - \sqrt{\left(R_a^2 + R_b^2 + L^2\right)^2 - 4\cdot R_a^2\cdot R_b^2}\right]\Big/2R_b^2\right\} \tag{34}$$

Using these relations along with conservation of energy, the shape factors with respect to inlet and outlet disk are given by Eqs. (35) and (36), respectively:

$$F_{k-\mathrm{ID}} = F_{k-a} - \sum_{i=1}^{k-1} F_{k-i} \tag{35}$$

$$F_{k-\mathrm{OD}} = F_{k-b} - \sum_{i=k+1}^{N} F_{k-i} \tag{36}$$

Inlet Disk to Outlet Disk

Using the law of conservation of energy and shape-factor relations developed in the preceding section, the shape factor between inlet and outlet disk is obtained as

$$F_{\mathrm{ID-OD}} = 1 - \sum_{l=1}^{k-1}\left[\left(\frac{A_k}{A_{\mathrm{ID}}}\right)\cdot F_{k-\mathrm{ID}}\right] \tag{37}$$

Figures 6 and 7 show shape-factor values for various cases obtained by solving the equations stated earlier. Graphs plotted in Fig. 6 are for the first element on the jet pipe, convergent section, and divergent section of nozzle, respectively. There are two peaks for the divergent section element, because the shape factor decreases rapidly in the convergent section (negative slope), but increases slightly when the last element of the jet pipe is visible. Similar peaks and discontinuity are observed in Fig. 7.

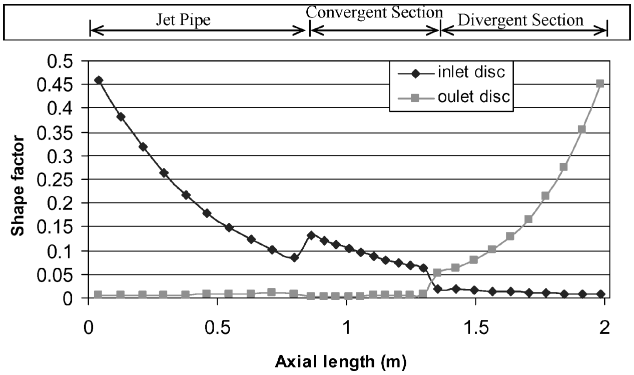

Fig. 7 Ring-element-to-inlet- and outlet-disk shape factors for jet pipe with C–D nozzle.

Radiation Shape-Factor Analysis for Annular Ducts

For the annulus (radiation shield and fuselage), all elements are either partially visible or totally invisible to each other. Compared to the previous case of jet pipe with C–D nozzle, the added complexity in finding shape factors of annular ducts with varying cross section is that the blocking section (one that blocks the larger view) for every pair of ring elements has to be evaluated. Various cases that are required are as follows.

Ring Element to Any Other Ring Element

These shape factors are obtained as

$$F_{1-2} = (-1)^m\cdot[G(\phi_o) - G(\phi_i)] \tag{38}$$

where $m = 2$ if both ring elements are on the inner or outer surface of ducts, else $m = 1$, and $G(\phi)$ is given by Eq. (26). The integration limits are determined by light-ray projection of blocking sections (Fig. 8) and are given by the following equations:

$$\phi_i = \pi - \max\left\{\cos^{-1}\left[\left(r_1^2\cdot x_2^2 - r^2\cdot x^2 + r_2^2\cdot x_1^2\right)\Big/(2r_1\cdot r_2\cdot x_1\cdot x_2)\right]\right]\right\}_i \tag{39a}$$

$$\phi_o = \pi - \max\left\{\cos^{-1}\left[\left(r_1^2\cdot x_2^2 - r^2\cdot x^2 + r_2^2\cdot x_1^2\right)\Big/(2r_1\cdot r_2\cdot x_1\cdot x_2)\right]\right]\right\} \tag{39b}$$

Figure 8 illustrates the blockage effect while evaluating the shape factor for radiation-shield inner surface element to fuselage inner-surface element for layout 1 (see Fig. 1). The presence of the inner duct (jet pipe and C–D nozzle) introduces blockage; besides, the elemental area on the emitter can see the receiver through the annular aperture formed at the radiation-shield exit (i.e., the radiation shield itself produces the blockage effect, which is referred to as blockage on the outer surface). Blockage due to the inner duct sets the upper integration limit, and blockage on the outer surface sets the lower integration limit (Fig. 8). These integration limits are found by projecting the blocking section onto the plane of the receiver element and using the laws of the triangle.

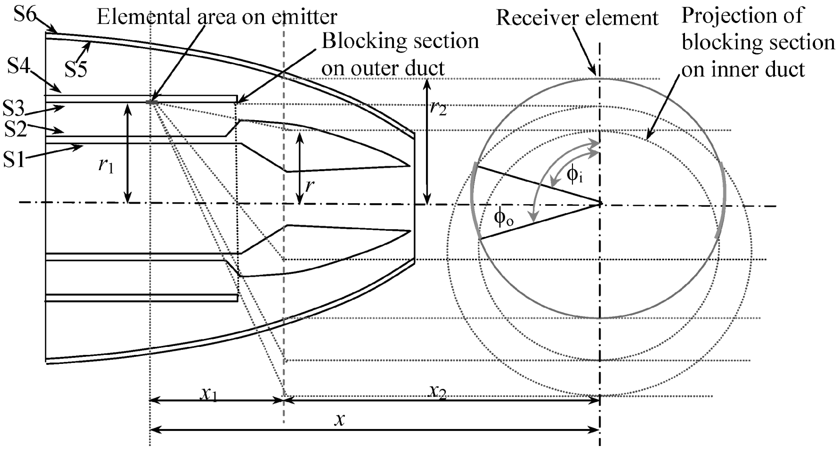

Fig. 8 Blockage effect in annular ducts: S1, jet pipe inner surface; S2, jet pipe outer surface; S3, radiation shield inner surface; S4, radiation shield outer surface; S5, rear fuselage inner surface; and S6, rear fuselage outer surface.

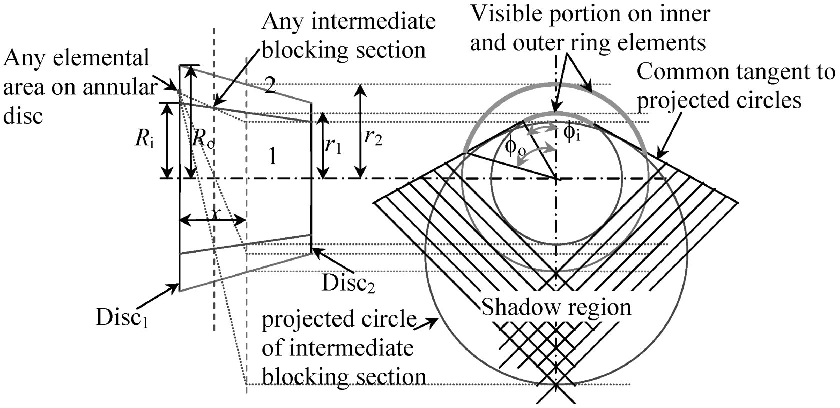

Fig. 9 Generalized elements in the annulus region.

Ring Element with Itself

Such shape factors are evaluated using annular-disk-to-ring shape factor, conservation of energy, and shape-factor algebra. The annular disk to ring element shape factor is obtained by the integration given in Eq. (40). This integral is derived from the basic quadruple line integral definition of the shape factors and can be solved numerically:

$$F_{\text{disk}-\text{element}} = (-1)^m \cdot \left[\left(\frac{2\pi}{A_{\text{disk}}}\right) \cdot \int_{R_i}^{R_o} e \cdot (g + h \cdot i) \cdot \mathrm{d}r_{\text{disk}}\right] \tag{40a}$$

where

$$a = (r_{\text{element}} - x \cdot \tan \eta_{\text{element}})/r_{\text{disk}} \tag{40b}$$

$$b = \left[r_{\text{element}}^2 + x^2 + r_{\text{disk}}^2\right] \big/ (2r_{\text{disk}} \cdot r_{\text{element}}) \tag{40c}$$

$$c = x^2 \big/ (\pi r_{\text{element}}) \tag{40d}$$

$$d = f \cdot \{1 + [\tan(\varphi/2)/f]^2\} \tag{40e}$$

$$e = c \cdot (a + 1)/(b + 1)^2 \tag{40f}$$

$$f = \sqrt{(b - 1)/(b + 1)} \tag{40g}$$

$$g = \{\tan^{-1}[\tan(\varphi/2)/f]\}/f]\}/f \tag{40h}$$

$$h = f^3/2 \tag{40i}$$

$$i = \tan^{-1}[\tan(\varphi/2)/f] + \tan(\varphi/2)/d \tag{40j}$$

In this integral, ϕ for the inner and outer frustum of the cone element (Fig. 9) is given by Eq. (41). The expression for ϕ is found by the shadowing technique; the shadow is the region of obscuration when a solid is illuminated from a point light source. In this case, the solid corresponds to the intermediate blocking segment, and the obscuration region is obtained by projecting each of the intermediate blocking sections in the segment on to the plane of the receiver, which is the region bounded by the common tangents to the projected circles of any intermediate blocking section and the inner ring element:

$$\phi_i = \cos^{-1}[(r_1 - x \cdot \tan \eta_1)/r_{\text{disk}}] \tag{41a}$$

$$\phi_o = \pi - \sin^{-1}(R_i/r_{\text{disk}}) - \sin^{-1}(r_1/r_2) \tag{41b}$$

Using the annular-disk-to-ring-element shape factors, shape-factor algebra, and the fact that the inner-duct outer surface is convex (i.e., $F_{1-1} = 0$), other shape factors can be obtained as follows:

$$F_{1-2} = 1 - (A_{\text{disk}_1}/A_1) \cdot F_{\text{disk}_1-1} - (A_{\text{disk}_2}/A_1) \cdot F_{\text{disk}_2-1} \tag{42a}$$

$$F_{2-1} = (A_1/A_2) \cdot F_{1-2} \tag{42b}$$

$$F_{2-2} = 1 - F_{2-1} - (A_{\text{disk}1}/A_2) \cdot F_{\text{disk}1-2} - (A_{\text{disk}2}/A_2) \cdot F_{\text{disk}2-2} \tag{42c}$$

Ring Element to Inlet and Outlet Disks

These shape factors are found on similar lines adopted for a jet pipe with a C–D nozzle. The only difference is that the number of visible surfaces is more than one and varies from element to element (viz., the last element on the C–D nozzle outer surface can see only the fuselage inner surface, but the element on the radiation-shield

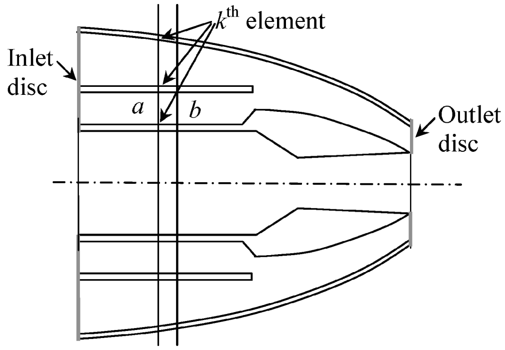

Fig. 10 Geometry of annular ducts.

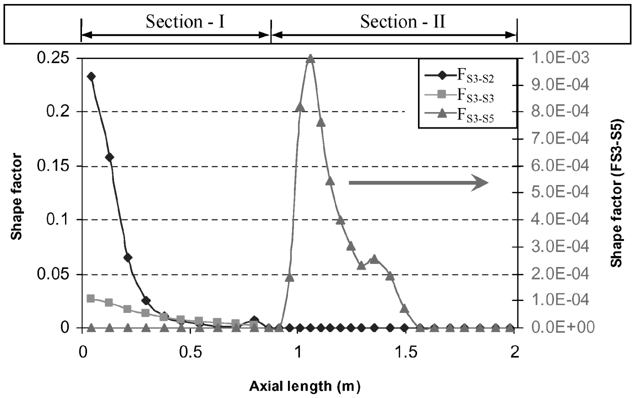

Fig. 11 Shape factors for ring element on radiation-shield inner surface for layout 1.

inner surface sees the inner surface of the radiation shield, fuselage, jet pipe, and C–D nozzle outer surface). Equations (43a) and (43b) give these expressions (Fig. 10):

$$F_{k-\mathrm{ID}} = F_{k-a} - \sum_{\text{surfaces}} \left(\sum_{i=1}^{k-1} F_{k-i} \right) \tag{43a}$$

$$F_{k-\mathrm{OD}} = F_{k-b} - \sum_{\text{surfaces}} \left(\sum_{i=k+1}^{N} F_{k-i} \right) \tag{43b}$$

Inlet Disk to Outlet Disk

This shape factor is derived along similar lines, as explained in the preceding section, and Eq. (44) gives the expression

$$F_{\mathrm{ID-OD}} = 1 - \sum_{\text{surfaces}} \left[\sum_{i=1}^{k-1} \left(\frac{A_k}{A_{\mathrm{ID}}} \cdot F_{k-\mathrm{ID}} \right) \right] \tag{44}$$

Figures 11 and 12 give the shape factors for various cases in layout 1 (see Fig. 1). Figure 11 is for the first element on the radiation-shield inner surface. The peak observed for F_{S3-S5} is because only a few elements of the fuselage inner surface are visible to the first element of the radiation-shield inner surface through the narrow slit between the radiation shield and the jet pipe. Figure 12 gives the shape factor of the 15th element of the rear-fuselage inner surface with other surfaces. The small peak observed at around 0.63 m in Fig. 12b is due to the visibility of the jet-pipe outer surface to the 15th element of the rear fuselage from the slit between the radiation shield and jet pipe.

Heat Balance and Numerical Accuracy

The most important way to validate results obtained from this thermal model is to check for energy, mass, and momentum balance. The ambient and ram air are radiative and convective heat sinks, respectively. Although exhaust gas is the main heat source, the freestream may act as a convective heat source or sink, depending on the flight altitude Mach number. The heat-balance equation for the system is given by

$$\sum_{k=1}^{N} \left[(\dot{m} \cdot C_p \cdot \Delta T_0)_{F\mathrm{I}} + (\dot{m} \cdot C_p \cdot \Delta T_0)_{F\mathrm{II}} + (\dot{m} \cdot C_p \cdot \Delta T_0)_{F\mathrm{III}} + \dot{q}_{\mathrm{CFIV}W\mathrm{III}} + \sum_{\text{surf}=1}^{6} (\dot{q}_r) \right]_k = 0 \tag{45}$$

The gasdynamic equations used to obtain temperature, pressure, and Mach number are derived from conservation of mass, momentum, and energy[21]; also, wall heat balance equations are solved to determine the wall temperatures. Thus mass and momentum balance for the system is implicit; however, heat balance for the system is carried out, and the percentage error in heat balance with respect to enthalpy drop in exhaust gases does not exceed 0.002%. Hence, the results obtained are fairly accurate. A convergence criterion of 1×10^{-4} is used for the wall temperature, and a criterion of 10^{-3} is used for the heat balance.

The integral for evaluating the shape factor of the annular disk to the ring element [Eq. (40)] is obtained by Simpson's $\frac{3}{8}$ rule. All shape factors obtained are checked by the summation rule, wherein the summation of the shape factor of an element with respect to all other elements and itself is unity (which follows from the law of energy conservation). The order of error in the summation rule varies from 10^{-7} to 10^{-3}.

Results

Figures 13 and 14 show temperature distribution over duct walls obtained from the combined radiative- and convective-heat-transfer

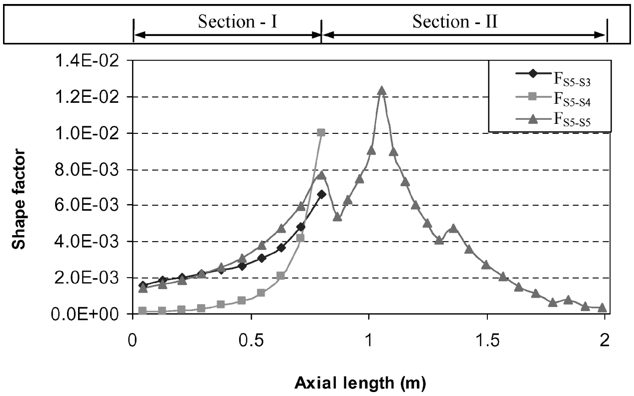

a) F_{S5-S3}, F_{S5-S4}, F_{S5-S5}

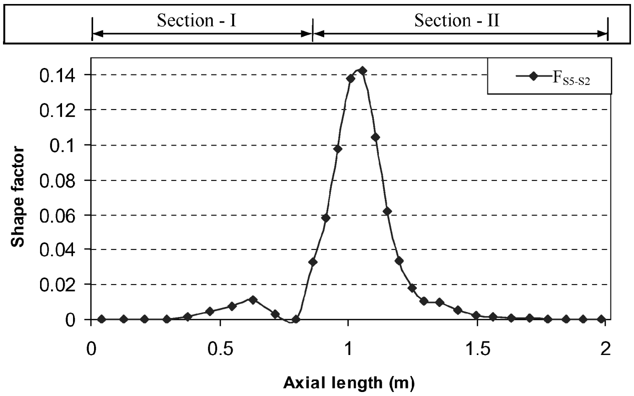

b) F_{S5-S2}

Fig. 12 Shape factors for ring element on rear-fuselage inner surface for layout 1.

model for layouts 1 and 2 (see Figs. 1 and 2), respectively. The results are obtained for a flight Mach number of 0.6 at an altitude of 2 km. The rear-fuselage operating temperature is higher in layout 1, because the rear fuselage is directly exposed to the hot nozzle. Also, the convective heat loss from the nozzle in layout 1 is less than in layout 2, because the nozzle section in layout 1 is in contact with low-velocity fluid, due to adiabatic mixing of fluids II and III.

The temperature profile of the three fluids (core exhaust gases and two ram airflows) is in Fig. 15. The core exhaust gases undergo a large variation in temperature; hence, there is a need to model the variation in thermophysical and transport properties of the fluid with temperature. Temperature distribution obtained by Mahulikar[9] is in Fig. 16. By comparison with Fig. 14, the difference in temperature estimation and the nature of the predicted temperature profiles is seen. This difference is because of the assumptions made in Mahulikar[9] (e.g., ignoring variation in thermophysical properties of fluid and aerodynamic heating of rear fuselage, and the approximation of coaxial cylinders).

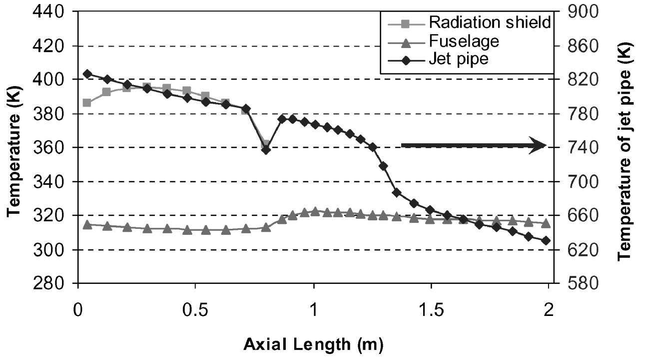

Fig. 13 **Temperature profile obtained from combined convection and radiation model for layout 1.**

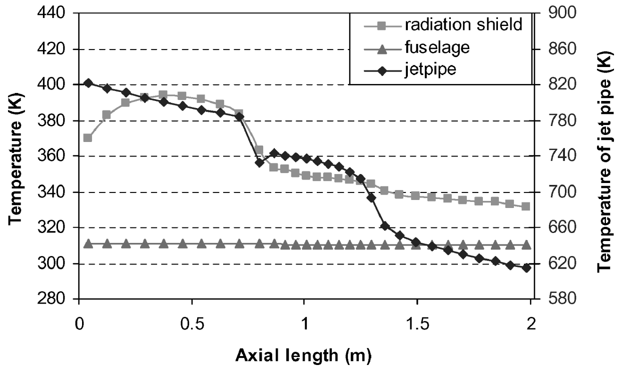

Fig. 14 **Temperature profile obtained from combined convection and radiation model for layout 2.**

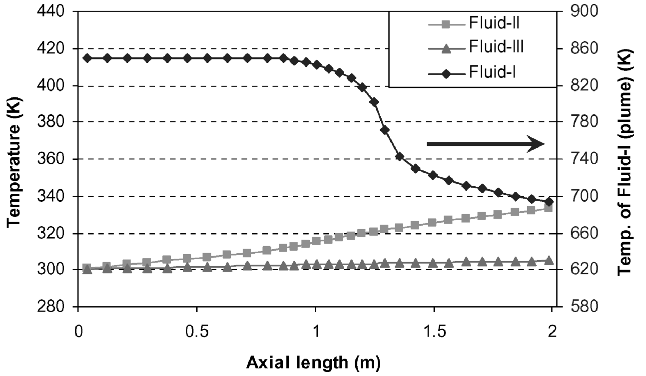

Fig. 15 **Temperature profile of the three fluids in layout 2.**

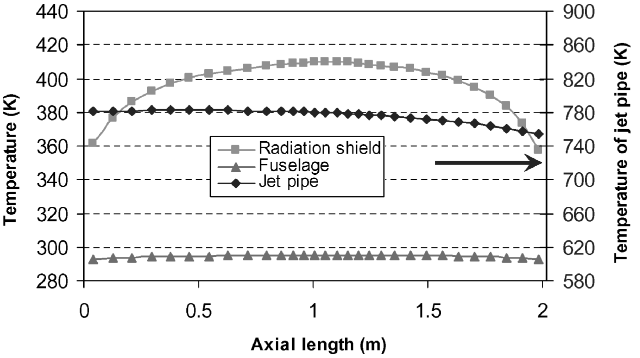

Fig. 16 **Temperature profile obtained for three coaxial cylinders by Mahulikar.[9]**

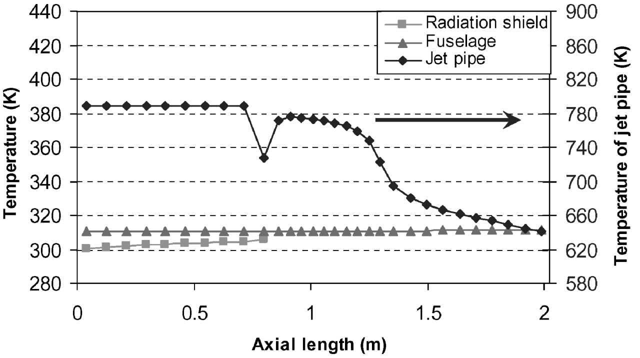

Fig. 17 **Temperature profiles obtained from turbulent forced-convection model for layout 1.**

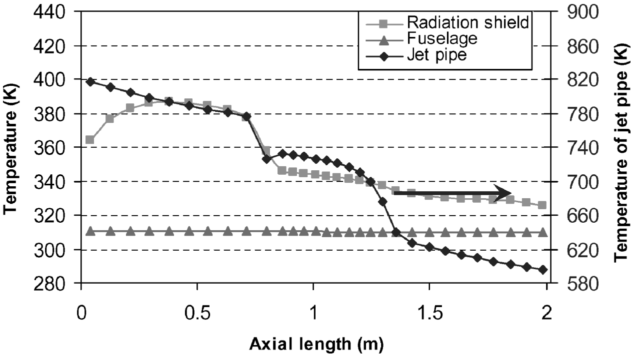

Fig. 18 **Temperature profile obtained from combined convection and radiation model for layout 2, ignoring variation in properties.**

The temperature distribution over duct wall surfaces for layout 1 using only the turbulent forced-convection model is in Fig. 17. After comparison with Fig. 13, it is clear that temperature distribution is significantly different if surface radiation interchange is neglected. This emphasizes the need to model surface radiation interchange of the actual geometry for temperature prediction in infrared signature studies. Accounting for the variation in fluid properties with temperature has a significant effect on the overall temperature distribution, especially for a jet pipe with a C–D nozzle, because the temperature of combustion gases flowing through the core is high and the gases undergo wide temperature variation (see Fig. 15), which is substantiated by comparing Figs. 18 and 14.

Figure 19 shows the temperature distribution obtained by ignoring the effect of heat generation in the boundary layer (aerodynamic heating) over the rear fuselage, which is found to be about 20 K lower than that in Fig. 14. The difference increases with flight speed, and because infrared (IR) power emitted by the fuselage is proportional to the sixth power of temperature in the band 3–5 μm (see Ref. 1),

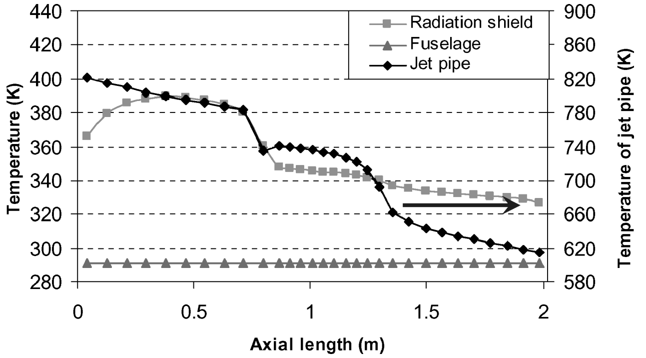

Fig. 19 Temperature profile obtained for layout 2, ignoring aerodynamic heating of rear fuselage.

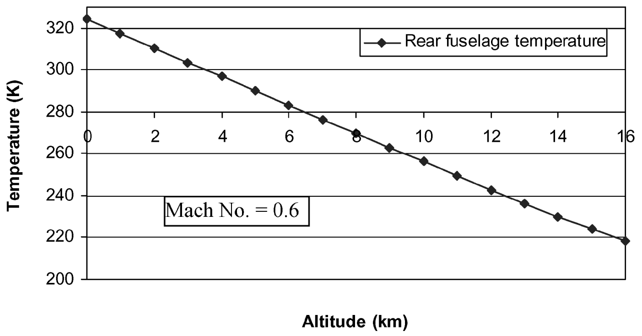

Fig. 20 Effect of altitude on rear-fuselage casing temperature.

ignoring aerodynamic heating can lead to substantial error in evaluation of IR signatures. Figure 20 shows the decrease in rear-fuselage temperature with increased aircraft altitude, because the ambient temperature of the atmosphere decreases linearly with altitude up to 16 km. Also, the convective-heat addition to the rear fuselage decreases, due to lower mass-flow rates in the engine.

Aerodynamic heating of the airframe occurs at all speeds (as the temperature in the boundary layer is always higher than that of the freestream) and is a heating source for the airframe. In case of the rear fuselage, the power plant is always the heat source. Even if heat is generated in the boundary layer, the freestream acts as a convective heat sink. It is only at very high Mach numbers that the freestream acts as a heat source, owing to higher recovery temperature. Hence, for aircraft with fuselage-embedded engines, the aerodynamic heating of the rear fuselage occurs only when the freestream starts acting as a heat source instead of a convective heat sink. This transition of the freestream is dictated by flight Mach number and altitude; transition altitude and transition Mach number are defined below. At transition, the rear-fuselage wall behaves like an adiabatic wall.

Definition: Transition altitude is the altitude at which transition of the freestream from heat sink to heat source occurs when flight Mach number is kept constant and flight altitude is decreased.

Definition: Transition Mach number is the Mach number at which transition of the freestream from heat sink to heat source takes place when the Mach number is increased and the altitude is kept constant.

Figure 21 shows variation of transition Mach number with flight altitude. The variation is approximated by a second-order polynomial (shown by the solid line in figure), because the recovery temperature varies with the square of the Mach number. The rear-fuselage-casing temperature depends on the freestream recovery temperature, which in turn varies with the square of the flight Mach number. Hence, the variation of the rear-fuselage temperature with the Mach number is nonlinear (Fig. 22). Here, two cases are considered. In one case, the freestream flow is calculated after an oblique shock (in supersonic flights), whereas it is neglected in the other case. The heat-transfer coefficient increases after the shock, because of increase in Prandtl number across the shock. Hence, aerodynamic-heating effect (at operating altitudes lower than the transition altitude) is enhanced, and the temperature of the rear fuselage obtained is slightly higher than as when freestream flow is modeled after the shock. As shown in Fig. 22, the effect is not significant, but increases with flight Mach number.

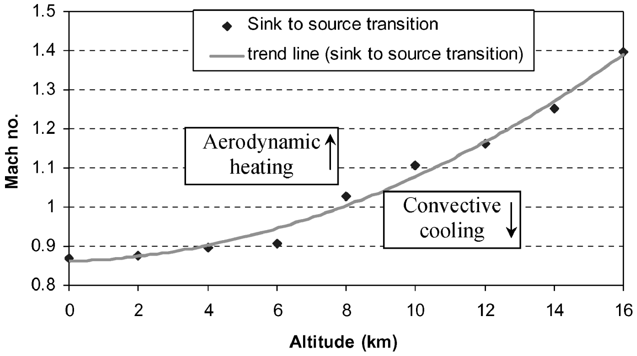

Fig. 21 Combined effect of altitude and Mach number.

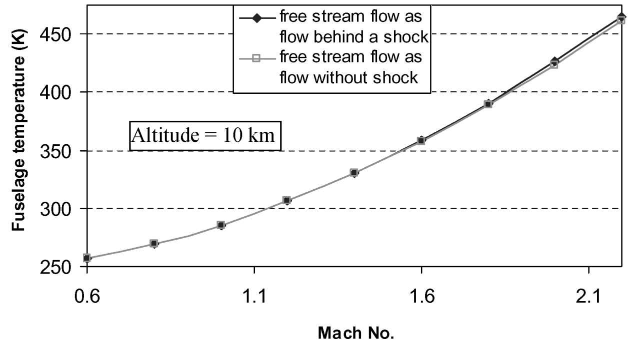

Fig. 22 Effect of flight Mach number on rear-fuselage casing temperature.

Conclusions

1) Closed-form solution for radiative shape factor from ring element (cylinder or frustum of cone) to ring element in annulus is derived, which can be applied to elements with small axial width.

2) Neglecting variation of fluid-transport properties with temperature, or aerodynamic heating of rear fuselage, introduces significant error in overall temperature distribution, which is critical for infrared signature studies.

3) For actual geometry of layout, the local flow properties vary significantly. Also, the shape factors are different from those for coaxial cylindrical ducts. Hence, approximating the aircraft rear-fuselage engine-layout geometry as coaxial cylindrical ducts can lead to errors in temperature predictions, for infrared signature studies. Thus, modeling surface radiation interchange for complex geometries is certainly worth the complexity.

4) Above the transition Mach number, the contrast (IR signature) with the rear fuselage is lower, compared to the contrast with the rest of the airframe (subject to comparison of contrast per unit solid angle subtended at the IR detector), owing to lower operating temperature of exposed casing, because of ram air cooling (additional convective heat sink).

5) Below the transition Mach number, the contrast with the rear fuselage would be greater than that with the rest of the airframe, owing to higher operating temperature as a result of power-plant heat sources. Similarly, above the transition altitude, contrast with the rear fuselage would be greater than with the rest of the airframe, and vice versa.

Acknowledgments

The authors express their gratitude to the Aeronautics Research and Development Board (Propulsion Panel), Ministry of Defense, Government of India, for financial support. The authors express their heartfelt gratitude to the reviewers of *Journal of Thermophysics and Heat Transfer* for the extremely valuable suggestions for modifying the manuscript. The authors sincerely appreciate the prompt, diligent processing of this paper by Richard Buckius, Associate Editor. The authors are grateful to S. K. Sane and A. G. Marathe for the encouragement for this investigation. The authors also thank the A. von Humboldt Foundation, Germany, for the rich exposure to research.

References

[1] Rao, G. A., and Mahulikar, S. P., "Integrated Review of Stealth Technology and Its Role in Airpower," *Aeronautical Journal*, Vol. 106, No. 1066, 2002, pp. 629–641.

[2] Bankston, C. A., and McEligot, D. M., "Turbulent and Laminar Heat Transfer to Gases with Varying Properties in the Entry Region of the Circular Ducts," *International Journal of Heat and Mass Transfer*, Vol. 13, No. 2, 1970, pp. 319–344.

[3] Malik, M. R., and Pletcher, R. H., "Computation of Annular Turbulent Flows with Heat Transfer and Property Variations," *Proceedings of 6th International Heat Transfer Conference*, Vol. 2, Hemisphere, Washington, DC, 1978, pp. 537–542.

[4] Pletcher, R. H., "Survey of Finite-Difference Strategy for Predicting Heat Transfer in Turbulent Channel Flows," *Turbulent Forced Convection in Channels and Bundles*, edited by S. Kakac and D. B. Spalding, Vol. 1, Hemisphere, Washington, DC, 1979, pp. 27–49.

[5] Pletcher, R. H., and Malik, M. R., "Prediction of Turbulent Flow Heat Transfer in Annular Geometries," *Turbulent Forced Convection in Channels and Bundles,* edited by S. Kakac and D. B. Spalding, Vol. 1, Hemisphere, Washington, DC, 1979, pp. 185–205.

[6] Stasiek, J., and Collins, M. W., "Radiant and Convective Heat Transfer for the Flow of an Optically Active Gas in a Cooled Wall with a Gray Wall," *Proceedings of the 9th International Heat Transfer Conference*, Vol. 6, edited by G. Hetsroni, Hemisphere, Washington, DC, Jerusalem, 1990, pp. 409–414.

[7] Smith, T. F., and Clausen, C. W., "Radiative and Convective Heat Transfer for Tube Flow of Real Gas," *Proceedings of 6th International Heat Transfer Conference*, Vol. 3, Hemisphere, Washington, DC, 1978, pp. 391–396.

[8] Mahulikar, S. P., Sane, S. K., Gaitonde, U. N., and Marathe, A. G., "Numerical Studies of Infrared Signature Levels of Complete Aircraft," *Aeronautical Journal*, Vol. 105, No. 1046, 2001, pp. 185–192.

[9] Mahulikar, S. P., "Prediction of Engine Casing Temperature of Fighter Aircraft for Infrared Signature Studies," *Proceedings of SAE's Aerospace Atlantic Conference*, Society of Automotive Engineers, Warrendale, PA, 1992.

[10] Eddy, T. L., and Neilsson, G. E., "Radiation Shape Factors for Channels with Varying Cross Sections," *Journal of Heat Transfer*, Vol. 110, No.1, 1988, pp. 264–266.

[11] Robin, W. H., "An Analysis of Thermal Radiation Heat Transfer in a Nuclear-Rocket Nozzle," NASA TN-D-586, Jan. 1961.

[12] Tso, C. P., and Mahulikar, S. P., "View Factors Between Finite Length Rings on an Interior Cylindrical Shell," *Journal of Thermophysics and Heat Transfer*, Vol. 13, No. 3, 1999, pp. 375–379.

[13] Reid, R. L., and Tennant, J. S., "Annular Ring Factors," *AIAA Journal*, Vol. 11, No. 10, 1973, pp. 1446–1448.

[14] Brockmann, H., "Analytical Angle Factors for the Radiant Interchange Among the Surface Elements of Two Concentric Cylinders," *International Journal of Heat and Mass Transfer*, Vol. 37, No. 7, 1994, pp. 1095–1100.

[15] Saltiel, C., and Naraghi, M. H. N., "Radiative Configuration Factors from Cylinders to Coaxial Axisymmetric Bodies," *International Journal of Heat and Mass Transfer*, Vol. 33, No. 1, 1990, pp. 215–218.

[16] Chung, B. T. F., Kermani, M. M., and Naraghi, M. H. N., "A Formulation of Radiation Shape Factors from Conical Surface," *AIAA Journal*, Vol. 22, No. 3, 1984, pp. 429–436.

[17] Modest, M. F., "Radiative Shape Factors between Differential Ring Elements in Concentric Axisymmetric Bodies," *Journal of Thermophysics and Heat Transfer*, Vol. 2, No. 1, 1988, pp. 86–88.

[18] Nunes, E. M., and Naraghi, M. H. N., "Numerical Model for Radiative Heat Transfer Analysis in Arbitrarily Shaped Axisymmetric Enclosures with Gaseous Media," *Numerical Heat Transfer*, *Part A*, Vol. 33, No. 5, 1998, pp. 495–513.

[19] Nunes, E. M., Modi, V., and Naraghi, M. H. N., "Radiative Transport in Arbitrarily Shaped Axisymmetric Enclosures with Anisotropic Scattering Media," *International Journal of Heat and Mass Transfer*, Vol. 43, No. 18, 2000, pp. 3275–3285.

[20] Cohen, H., Roger, G. F. C., and Saravanamuttoo, H. I. H., *Gas Turbine Theory*, Addison Wesley Longman, Essex, England, U.K., 1996, pp. 106–112.

[21] Emanuel, G., *Gas Dynamics*, *Theory and Applications*, AIAA, New York, 1986, pp. 113–118, 433.

[22] Sukhatme, S. P., *A Text Book on Heat Transfer*, 3rd ed., Orient Longman, Bombay, India, 1990, pp. 143–180.

[23] Truitt, R. W., *Fundamentals of Aerodynamic Heating*, Ronald, New York, 1960, pp. 106–107.

[24] Stoecker, W. F., *Design of Thermal Systems*, McGraw–Hill, New York, 1989, pp. 111–126.

[25] Ozisik, M. N., *Heat Transfer*, *A Basic Approach*, McGraw–Hill, Singapore, 1985, p. 632.